Applied Thermal Engineering 233 (2023) 121165

Contents lists available at ScienceDirect

Applied Thermal Engineering

journal homepage: www.elsevier.com/locate/apthermeng

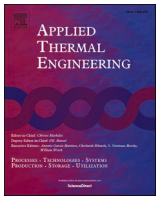

Research Paper

Experimental and numerical analysis of a CO_2 dual-source heat pump with PVT evaporators for residential heating applications

Emanuele Zanetti, Sara Bordignon, Riccardo Conte, Alberto Bisi, Marco Azzolin *, Angelo Zarrella

Department of Industrial Engineering, University of Padova, Via Venezia 1, 35131 Padova, Italy

ARTICLE INFO

Keywords:
Heat pump
Carbon dioxide
Direct expansion
Water heating
Numerical modeling
TRNSYS

ABSTRACT

Multi-source energy systems are a promising solution to lower the environmental impact of the heating and cooling sector and enhance the exploitation of renewable energy sources. In this context, dual-source solar-assisted heat pumps exploit solar energy and air as the low-temperature heat sources. However, the efficiency of solar-based systems is strictly related to weather conditions, location, and time. Therefore, there is a need for accurate models to be used in dynamic simulations of these systems and perform detailed performance analyses and study the involved energy flows.

This paper presents an experimental and numerical investigation of a direct-expansion solar-assisted heat pump (DX-SAHP) operating with CO_2 as the refrigerant. The heat pump prototype can work with an air-finned coil heat exchanger or photovoltaic-thermal (PVT) solar collectors as the evaporator. The solar-mode configuration allows the exploitation of the heat from solar radiation to evaporate the refrigerant and to improve the photovoltaic electricity production due to the cooling of the cells up to 8%.

A numerical heat pump model, integrated with novel gas-cooler and PVT collectors models, has been developed and implemented as a TRNSYS type for dynamic simulations of the system. The model has been validated with continuous measurements during the heat pump operation in solar and air modes. The proposed model can be used for performing seasonal simulations of a heat pump operating with a transcritical CO_2 cycle. Moreover, the outcomes of the analysis show how the configuration of a CO_2 heat pump with a direct-expansion air-finned coil heat exchanger or PVT can be used to enhance the performance of the heat pump and increase the electrical efficiency of the photovoltaic cells.

1. Introduction

Heat energy end-use accounts for almost 50% of global final energy consumption in 2021, of which 46% is consumed in buildings for space and water heating [1]. Fossil fuels account for 64% of global energy use for buildings-related heating, decreasing only three percentage points since 2010, and are responsible for 80% of direct CO_2 emissions in the building sector [2]. Heat pumps, powered by low-emissions electricity, are considered the central technology in the global transition to secure and sustainable heating [3]. According to Delegated Regulation (EU) 2022/759 [4], part of the aerothermal, geothermal, or hydrothermal energy captured by heat pumps is considered energy from renewable sources. In addition, a share of the electrical energy demanded by electrically driven heat pumps is produced using renewable primary energy sources, according to the national fuel mix [5]. In this context, integrating renewables and heat pumps becomes crucial in the transition to more sustainable air conditioning systems in residential and non-residential applications.

Nowadays, the research on heat pump technology is focused on the possible usage of environmentally friendly refrigerants with a low global warming potential (GWP) and on improving the system performance, reducing the consumption, or maximizing the thermal production, i.e., the coefficient of performance (COP). The adoption of low GWP refrigerants and the phase-down of hydrofluorocarbons (HFC) is pushed by the recent regulations (Regulation No 517 of European Union of 2014 [6] – and its new proposal, which is nowadays under review- and the Kigali Amendment of United Nations of 2016 [7]).

The use of CO_2 as the refrigerant is very promising due to its low global warming potential (GWP = 1), zero ozone-depleting potential (ODP), no toxicity, and no flammability (class A1 for ASHRAE). Furthermore, CO_2 provides high heat transfer coefficients and low

* Corresponding author.
E-mail address: marco.azzolin@unipd.it (M. Azzolin).

https://doi.org/10.1016/j.applthermaleng.2023.121165
Received 9 February 2023; Received in revised form 17 May 2023; Accepted 13 July 2023
Available online 20 July 2023
1359-4311/© 2023 The Author(s). Published by Elsevier Ltd. This is an open access article under the CC BY license (http://creativecommons.org/licenses/by/4.0/).

Nomenclature

Symbols

A	area [m^2]
a_x	finned coil evaporator efficiency empirical coefficients
b_{pv}	temperature coefficient of power [K^{-1}]
c_p	specific heat capacity [J kg^{-1} K^{-1}]
C_x	compressor polynomials empirical coefficients
D	internal diameter [m]
G	incident solar radiation [W m^{-2}]
GA	absorbed solar radiation [W]
h	specific enthalpy [J kg^{-1}]
H	global transmission coefficient [W m^{-2} K^{-1}]
htc	local heat transfer coefficient [W m^{-2} K^{-1}]
K	global heat transfer coefficient [W m^{-2} K^{-1}]
KA	heat transfer coefficient/exchange area product [W K^{-1}]
l	serpentine length [m]
$\dot{m}$	mass flow rate [kg s^{-1}]
n	number of discretized elements/node
N	number of plates [-]
P	electrical power [W]
p	pressure [bar]
Q	heat flow rate [W]
R	thermal resistance [m^2 K W^{-1}]
T	temperature [°C]
t	thickness [m]
v	wind velocity [m s^{-1}]

Greek symbols

α	absorption coefficient [-]
η	efficiency [-]
λ	thermal conductivity [W m^{-1} K^{-1}]
ρ	density [kg m^{-3}], reflection coefficient [-]
$\overline{\tau\alpha}$	ratio of absorbed solar radiation [-]
σ	Stefan-Boltzmann constant [W m^{-2} K^{-4}]
β	slope angle [°]
τ	transmission coefficient [-]

Subscripts/Superscripts

air	air
c	compressor
e	evaporation
fin	equivalent fin
gc	gas-cooler
g	glass
guess	tentative
HE	user heat exchanger
i	plate discretised element/iteration
in	inlet
dis	compressor discharge
int	internal heat exchanger
lam	throttling valve
m	measured value
max	maximum
out	outlet
p	plate
sky	equivalent sky
r	refrigerant
s	simulated value
suc	compressor suction
abs	absorber plate
T1	TANK1
T2	TANK2
tot	total
user	user load
w	water
EVA	ethylene vinyl acetate
ref	reference
pipe	refrigerant pipe
we	welding
start	starting value
node	PVT node

Acronyms /Abbreviations

PV	photovoltaic
PVT	photovoltaic-thermal collector
COMP	compressor
COP	coefficient of performance
GC	gas-cooler
INT	internal heat exchanger
EEV	electronic expansion valve
REC	low-pressure receiver tank
RMSE	root mean square error
USER	user heat exchanger
TANK	water tank
DX-SAHP	direct-expansion solar-assisted heat pump
GWP	global warming potential
HFC	hydrofluorocarbons
ODP	ozone-depleting potential
LCA	life cycle assessment
MPPT	maximum power point tracking

pressure drop compared to other refrigerants [8]. However, its low critical point and high operating pressure require careful attention in the design of the system components [9].

Besides the low environmental impact, one of the main advantages of carbon dioxide is the possibility of providing a high temperature lift between the water inlet and outlet when using a transcritical cycle. For this reason, the transcritical CO_2 cycle is particularly suitable for domestic water heating. Calise et al. [10] investigated the use of CO_2 heat pumps to replace conventional gas-fired boilers for heating in buildings. They carried out TRNSYS [11] simulations and explored the use of CO_2 heat pumps in applications where radiators are used, instead of low-temperature terminal units, and high water temperatures are needed.

Liu et al. [12] numerically demonstrated that, although the COP of a basic CO_2 transcritical cycle is lower than the COP of a comparative cycle operating with R134a, CO_2 systems can achieve higher energy efficiency with proper cycle modifications: two-stage compression, vapor injection, and inter-stage cooling. A further way to enhance the efficiency of heat pumps is to use different heat sources. For instance, solar-assisted heat pumps (SAHPs) exploit solar radiation as the low-temperature thermal source, leading to better performance compared to air-source heat pumps under high irradiance conditions [13]. SAHPs can be coupled to solar thermal collectors or photovoltaic-thermal collectors (PVT), which can simultaneously provide electrical and thermal power to the energy system [14,15]. Usually, the warm water from the solar field releases heat in the evaporator to the heat pump's refrigerant [13,16]. For example, Leonforte et al. [17] presented the results of the experimental monitoring on a PVT-coupled SAHP system to assess the daily and seasonal performance of the system providing heating, cooling, and DHW to a building. They tested the unit under different set point temperatures and building loads and showed how the investigated configuration can enhance the electrical and thermal efficiency of PVT collectors, maximizing the heat pump's seasonal performance and

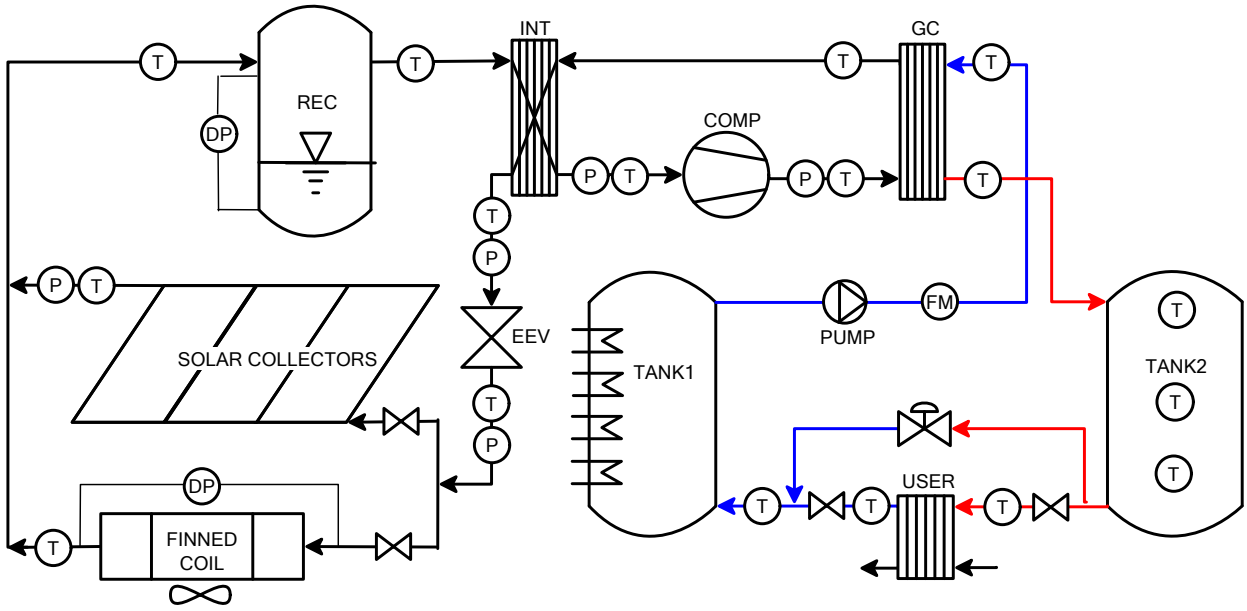

Fig. 1. Layout of the heat pump and water loop with the sensors installed: T temperature probe, P pressure transducer, FM Coriolis flowmeter, DP differential pressure.

reducing the electricity exchange with the electrical grid. Yu et al. [18] evaluated the performance of a direct-expansion SAHP with an evacuated tube collector-evaporator, experimentally testing the system under different operating conditions. In particular, they studied the effect of several parameters (i.e., the solar radiation intensity, circulating water temperature, ambient temperature, and collector area) on the thermodynamic and exergy performance of the system and identified the evacuated tube collector-evaporator and compressor as the parts of the system to be improved to increase the overall efficiency.

However, there are few experimental studies, in the available literature, on direct-expansion solar-assisted heat pumps for hot water production working with CO_2 as the refrigerant. Duarte et al. [19] experimentally investigated the operation of a small solar-assisted heat pump with a sheet-and-tube solar evaporator for hot water production. They found that the water inlet temperature strongly influences the gas-cooler outlet pressure and temperature. Paulino et al. [20] performed numerical simulations of the same system under dynamic conditions, studying the effect of solar radiation changes. To enhance the overall performance of direct-expansion solar-assisted heat pumps, the use of PVT solar collectors/evaporators is investigated in the literature [21,22]. The main advantage of using PVT evaporators is the possibility of simultaneous heat and electrical power production and improved photovoltaic conversion efficiency due to the cells cooling. Zhou et al. [23] experimentally and numerically investigated an R410A solar heat pump with micro-channel PVT modules as the evaporator. The results showed an average COP of the system between 4.7 and 5. Du et al. [22] realized a dual-source solar-assisted heat pump with R22 as refrigerant, operating with two PVT solar collectors, composed of micro heat pipe arrays applied on the PV back sheet and an additional finned air duct. During the tests at the same ambient conditions, the COP obtained in solar mode was 18.2% higher than in air mode.

None of the previous works addresses the direct expansion of CO_2 in PVT evaporators. To the authors' knowledge, only the experimental works by Zanetti et al. [24,25] investigated a CO_2 solar-assisted heat pump system working with a PVT evaporator. In the study, the performance coefficient of the dual-source heat pump (solar-air heat pump) can increase up to 30% in solar-source mode compared to the air-source mode.

The increase of the renewable share in the heating and cooling sectors and the consequent use of multi-source heat pumps makes it necessary to develop a strategy for the selection of the different thermal sources based on the environmental conditions, thermal load, and storage [26,27]. When addressing this problem, numerical tools can be useful to evaluate the performance of multi-source heat pumps and choose a source selection strategy. The prediction of the energy efficiency and evaluation of the energy flows in multi-source energy systems is usually made using dynamic energy simulation tools. Among the existing energy simulation tools, TRNSYS software is a flexible package of utility programs that enables the simulation and analysis of transient systems. It is a graphically based tool in which the different components of the system are interconnected and represented as black boxes called "Types", and it is often employed to analyze and investigate systems involving renewable energy sources and storage devices [28]. Generally, most of the analyses carried out with TRNSYS software use the performance matrix of commercial heat pumps to simulate their operating conditions [29]. This could lead to problems when unit details or its performance are missing or not provided by the manufacturers. Chargui et al. [30] modeled and simulated with TRNSYS a dual-source heat pump using air and ground as heat sources and CO_2 as the refrigerant. The investigated heat pump presented two evaporators: one for heat exchange with a water source (solar or geothermal) and one for heat exchange with the ambient air. Emmi et al. [15] developed a TRNSYS model of a solar-assisted ground source heat pump using a ground loop and a solar loop as the thermal source/sink, where the use of solar thermal collectors and PVT was investigated. The results proved the possibility of obtaining a relevant improvement in the heat pump's efficiency using PVT. Ma et al. [31] evaluated the performance variation of indirect-expansion SAHPs using CO_2 as the refrigerant for different configurations (one-stage and two-stage transcritical cycle) with solar thermal collector area, storage tank volume, and heat pump compressor capacity based on TRNSYS models. In this context, the availability of a heat pump TRNSYS type, for the dynamic modeling of a transcritical CO_2 thermodynamic cycle and simulating the operations with a conventional finned coil heat exchanger or PVT panels as the evaporator, is extremely interesting. Indeed, this would allow a more comprehensive and detailed analysis of the investigated energy system, providing information on the involved thermal and electrical energy flows and the energy performance at both unit and energy system levels.

Considering the reviewed literature, there is a lack of studies regarding the modeling of PVT evaporators working with CO_2 and

Fig. 2. Picture of the heat pump prototype, including finned coil evaporator and PVT collectors.

Fig. 3. Picture of the water tanks and the USER brazed plate heat exchanger.

Table 1
Main components of the heat pump system.

Component	Type	Characteristics
Compressor	Rotary, inverter driven	Displacement: 3.02 cm^3/rev
Gas-cooler	Brazed plate	Number of plates: 28 Plate size: 379 × 79 mm
Internal heat exchanger	Brazed plate	Number of plates: 4 Plate size: 377 × 120 mm
Throttling valve	Electronic	High-pressure control
Air evaporator	Finned coil	Number of circuits: 4 Number of tubes: 88 Tube internal diameter: 9.5 mm
Solar evaporator	PV-T collectors	Number of collectors: 3
Water storage	Cylindrical tank	Number of tanks: 2 Tank size: 200 L Heating elements: 4 resistances, 4.5 kW each

numerical models that consider the entire direct-expansion heat pump system and its coupling with the user water loop. Due to the lack of correlations describing the heat transfer of supercritical CO_2 in plate heat exchangers [32], there are no numerical models of plate gas-coolers, which are largely encountered in commercially available heat pumps.

The present work aims to cover this gap by studying a direct-expansion dual-source CO_2 heat pump experimentally and numerically. The main novelties are the followings:

- experimental tests conducted in dynamic conditions are presented when the dual-source CO_2 heat pump operates in air and solar modes under real environmental conditions;
- a model of the gas cooler based on a recent correlation developed for supercritical CO_2 is presented and compared with experimental data obtained during steady-state operations;
- a dynamic heat pump and water loop model has been developed using TRNSYS. The developed heat pump TRNSYS component includes the PV-T collectors model;
- the dynamic model has been compared and validated against the experimental data. It can be considered an important tool to assess the heat pump performance over long time and develop a control strategy to maximize the advantages of a dual-source system.

2. Heat pump prototype

The present dual-source (solar and air) CO_2 heat pump is installed at the University of Padova, Italy (45° 24′ 23″N, 11° 52 40″E), and it operates a transcritical cycle to produce hot water at the gas-cooler. The prototype has a heating capacity equal to 5 kW, and it has been designed to work alternatively with two evaporators: a finned coil air heat exchanger or 3 photovoltaic-thermal (PVT) solar collectors. The layout of the system with the sensors installed and the auxiliary water loops is shown in Fig. 1. When considering the refrigerant cycle of the heat pump, after an inverter-driven rotary compressor (named COMP in Fig. 1), the high-pressure superheated refrigerant is sent to the gas-cooler (GC), a brazed plate heat exchanger with water flowing in counter-current. After the gas-cooler, the refrigerant enters an internal heat exchanger (INT), where the CO_2 is cooled down. Subsequently, it is expanded into an electronic expansion device (EEV) that operates as a back-pressure valve to control the pressure at the gas-cooler. From this point, the refrigerant can evaporate inside the finned coil heat exchanger or the solar PVT collectors. After evaporation, the CO_2 enters the low-pressure receiver tank (REC), where the vapor phase is extracted from the top and sent to the compressor through the internal heat exchanger (which guarantees a certain degree of superheating at the compressor suction). During the heat pump operation, it has been possible to control the high-pressure value at the gas-cooler side, the compressor's speed, and the fan's velocity at the finned coil evaporator. Fig. 2 displays the casing of the heat pump prototype (containing the compressor, gas-cooler, internal heat exchanger, receiver, and expansion device), the finned coil evaporator, and the back of the three PVT collectors.

The water loop comprises two 200 L tanks and one brazed plate heat exchanger (named USER in Fig. 1) between the two tanks. The water exiting the cold tank (named TANK1) is sent to the gas-cooler using a water pump. The water is heated in the gas-cooler and enters the hot tank (TANK2). The user heat flow rate is drawn at the USER plate heat exchanger. It is also possible to modulate the mass flow rate in the USER heat exchanger acting on a bypass valve. Two valves placed before and after the USER heat exchanger allow to isolate this part of the circuit when there is no thermal load request by the user. In the TANK1, four variable electrical resistances, capable of producing up to 4.5 kW each, allow controlling the tank's temperature and, consequently, the water temperature at the inlet of the gas-cooler. During the experimental campaign, the temperature at the inlet of the gas-cooler was maintained at a temperature of about 30 °C. Fig. 3 shows a picture of the water loop with the two tanks and the USER brazed plate heat exchanger.

The refrigerant circuit and the water loop are thermally insulated to limit the heat losses towards the external ambient.

The main components of the system and their characteristics are listed in Table 1.

Table 2
Main characteristic of the PVT collector.

Characteristic	Value
Dimensions	1650 x 992 mm
Tilt angle	45°
Absorber thickness	0.5 mm
Tube thickness	1 mm
External tube diameter	8 mm
Tube pitch	80 mm
Number of tubes	15

Table 3
Uncertainty of sensors used.

Parameter	Sensor Type	Uncertainty
Temperature	T-type thermocouples	±0.1 K
Temperature	PT-100 resistance temperature detector	1/10 DIN
Pressure	Pressure transducers	±5 kPa
Solar irradiance	Secondary standard pyranometer	ISO 9060
Water mass flow rate	Coriolis effect flow meter	0.1% of the reading
Electric power	Power analyzer Norma 4000	0.1% of the reading

2.1. Heat exchangers

When the heat pump works with the air as the thermal source (hereafter air-mode), a conventional finned coil heat exchanger is used as the evaporator. The finned coil has 22 ranks and 4 rows, and the fluid flow is subdivided into 4 circuits made of 3.2 mm internal diameter tubes. The finned coil evaporator is coupled to a fan driven by a 0–10 Vdc signal to modulate the rotation speed.

When the heat pump works with solar radiation as the thermal source (hereafter solar-mode), three PVT solar collectors are used as the evaporator. Using a PVT device for this purpose has two benefits: exploiting the energy from solar radiation to evaporate the refrigerant flow and improving the PV electricity conversion by cooling the photovoltaic cells [24]. Each PVT collector comprises an aluminum plate (0.5 mm thickness) glued below a multicrystalline PV module. Each plate is coupled with an 8 mm external diameter copper serpentine. The PV modules are connected to a variable electrical resistance, allowing operating at the maximum power point (MPPT). The main features of the PVT collectors are reported in Table 2.

The gas-cooler is a brazed plate heat exchanger where water and CO_2 flow in a single pass/counter-current configuration. It consists of 28 plates with external dimensions of 379 × 79 mm.

An internal heat exchanger increases the temperature of the vapor CO_2 exiting the low-pressure receiver to supply the compressor with a certain degree of superheating by further cooling the CO_2 exiting the gas-cooler. The internal heat exchanger is a single pass/counter current brazed plate heat exchanger with 4 plates (the external dimensions are 377 × 120 mm).

2.2. Data reduction

The heat pump and the water circuit have been equipped with several sensors (see Fig. 1).

In the heat pump system, temperature sensors (T-type thermocouples) and pressure transducers have been placed at the inlet/outlet of each component. One differential pressure transducer has been used to evaluate the pressure drop inside the finned coil heat exchanger. The air temperature has been assessed with a PT-100 resistance temperature detector, and the solar irradiance on the tilt angle of the PVT collectors has been evaluated with a secondary standard pyranometer. One cup anemometer has been used to measure the wind velocity. The compressor power consumption (including the inverter), the heat pump's global power consumption, and the power produced by the photovoltaic modules have been measured by a power analyzer Norma 4000.

In the water loop, the water mass flow rate has been measured using a Coriolis effect mass flow meter, while the water temperatures at the inlet/outlet of the gas-cooler have been measured with two PT-100 s placed inside two thermowells. Three thermocouples have been placed in thermowells at different heights of the TANK2 to evaluate the water thermal stratification in the tank. Two thermocouples have been used to measure the water temperature at the inlet/outlet of the USER heat exchanger, and one thermocouple to measure the water temperature before entering TANK1.

The heating capacity produced at the gas-cooler can be calculated with an energy balance on the water-side:

$$Q_{gc} = \dot{m}_w c_p \left(T_{out_{gc},w} - T_{in_{gc},w}\right) \quad (1)$$

where $\dot{m}_w$ is the water mass flow rate measured by the Coriolis flowmeter, c_p is the water specific heat capacity and $\left(T_{out_{gc},w} - T_{in_{gc},w}\right)$ is the difference between the water temperatures measured at the outlet/inlet of the gas-cooler.

Considering the USER heat exchanger and the bypass line as a black box, the heat flow rate delivered to the user can be calculated with the following equation:

$$Q_{user} = \dot{m}_w c_p \left(T_{out_{T2}} - T_{in_{T1}}\right) \quad (2)$$

where $\left(T_{out_{T2}} - T_{in_{T1}}\right)$ is the difference between the temperature measured at the inlet of the USER heat exchanger (i.e., at the outlet of TANK2) and the temperature measured before entering TANK1.

A data logger Agilent 34970 continuously records all the data with a time step equal to 10 s.

The uncertainties of the sensors are reported in Table 3.

The combined uncertainty for non-measured data has been calculated following the law of error propagation according to [33]. The average uncertainty of the heating capacity (Q_{gc}) was equal to 0.44% when the temperature drop across the gas-cooler was higher than 10 K, whereas the average uncertainty of the user thermal load (Q_{user}) was equal to 0.57% when the temperature drop across the user heat exchanger was higher than 10 K.

3. Numerical model

3.1. Trnsys model

Fig. 4 shows a scheme of the system modeled in the TRNSYS environment. In Fig. 4, the blue lines highlight the water loop of the system. Water is pumped using a circulator (Type 3d), and the stream is warmed inside the heat pump's gas-cooler. After this, the water flow rate enters TANK2 (Type 534) from the upper part while the outlet of the thermal storage is located in the bottom part. The water, exiting TANK2, flows into a diverter that can convey the fluid directly to the mixing valve or to the plate heat exchanger to meet the USER thermal load. After the mixing valve, the total water stream is sent to TANK1, and then the flow rate is delivered to the circulation pump, closing the loop.

The inputs to the model are:

- the thermal load to be provided to the user;
- the heat exchanger inlet and outlet well water temperatures;
- the total water flow rate circulating in the system;
- the external air temperature;
- the supply voltage of the compressor, throttling valve, and fan;
- the power of the electrical resistances in the TANK1.

The flow diverter and plate heat exchanger are simulated using simple equations. The flow rate delivered to the heat exchanger ($\dot{m}_{HE}$) is

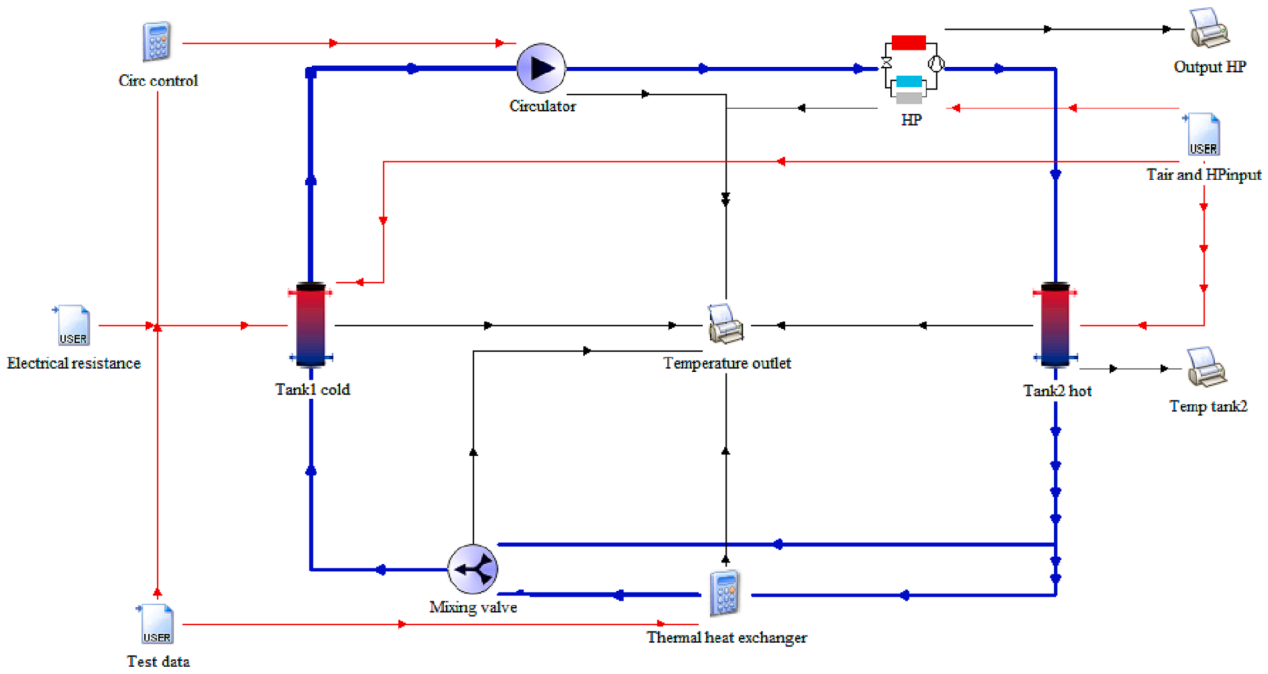

Fig. 4. Scheme of the system modeled in Simulation Studio.

calculated using the real temperature difference of the well water between the heat exchanger's inlet and outlet and the thermal load measured during the experimental campaign.

$$\dot{m}_{HE} = \frac{Q_{user}}{c_p \left(T_{out_{T2_m}} - T_{out_{HE_m}}\right)} \tag{3}$$

where Q_{user} is the user's thermal load, $T_{out_{HE_m}}$ and $T_{out_{T2_m}}$ are the temperatures at the outlet of the USER heat exchanger and the TANK2, respectively.

Once the mass flow rate value through the heat exchanger is computed, the temperature at the outlet of the heat exchanger is calculated using the modeled temperature at the inlet.

$$T_{out_{HE_s}} = T_{out_{T2_s}} - \left(\frac{Q_{user}}{c_p \ \dot{m}_{HE}}\right) \tag{4}$$

where $T_{out_{T2_s}}$ is the temperature at the outlet of TANK2 calculated by the model.

3.2. Heat pump model

The heat pump has been modeled by creating a specific TRNSYS type (HP in Fig. 4), adapting the heat pump TRNSYS type described in [29] to the actual heat pump prototype. The numerical model of the heat pump is based on an iterative algorithm to solve the supercritical carbon dioxide cycle under different external conditions and operative modes. The base algorithm to model the heat pump was presented by Zanetti et al. [24]; however, a novel approach has been used to model the gas-cooler and the PVT collectors for the numerical tool described in this work. The HP type can calculate the heat pump's energy fluxes and performance indicators given the environmental conditions, the compressor speed, and the high-pressure value.

The model simulates the steady-state operation of the unit since its transient operation is negligible compared to the inertia of the water storage tanks. The following assumptions have been made:

- the pressure drop in the heat exchangers is neglected;
- the heat exchangers and compressor are adiabatic;
- the high-pressure value is a model input since it can be selected through the back-pressure expansion device.

The Refprop [34] subroutine is used to calculate the intermediate fluid properties in the model.

The solution algorithm of the refrigerant cycle is realized through the following steps (Zanetti et al. [24]):

- First, tentative values of the evaporation temperature T_e and pressure p_e are assumed based on the environmental conditions. As demonstrated by Zanetti et al. [24], in the present heat pump prototype, the CO_2 exits the evaporators as saturated vapor (vapor quality between 0.94 and 1) in any operating condition. Therefore, in the model, the vapor quality at the evaporator outlet is constant and equal to 1, and the enthalpy $h_{out,e}$ can be calculated as a function of the evaporation temperature.
- The refrigerant mass flow rate ($\dot{m}_r$), the compressor power consumption (P_{tot}), and the specific compressor work ($h_{dis} - h_{suc}$) are calculated through a 20 coefficients polynomial, depending on the evaporation temperature, the pressure at the gas-cooler and the compressor speed, similar to the standards [35,36]. The polynomial equations with the experimental coefficients, derived from empirical data, are reported in Appendix A.
- The refrigerant temperature at the gas-cooler outlet $T_{out_{gc,r}}$ is calculated through the gas-cooler model (see 3.2.1).
- The energy balance at the internal heat exchanger is solved with the mean logarithmic temperature difference method:

$$Q_{int} = (KA)_{int} \frac{\left(T_{out_{gc,r}} - T_{in,c}\right) - \left(T_{in,lam} - T_{out,e}\right)}{\log\left(\frac{T_{out_{gc,r}} - T_{in,c}}{T_{in,lam} - T_{out,e}}\right)} \tag{5}$$

In Eq. (5) the overall heat transfer coefficient/exchange area product $(KA)_{int}$ has been derived from the experimental data in a linear equation as a function of the refrigerant mass flow rate [24]:

$$(KA)_{int} = 1011.6 \ \dot{m}_r - 2.1987 \tag{6}$$

An updated value of the refrigerant conditions at the outlet of the internal heat exchanger ($h_{in,lam}$) can thus be calculated:

$$h_{in,lam} = h_{out,lam} + \frac{Q_{int}}{\dot{m}_r} \tag{7}$$

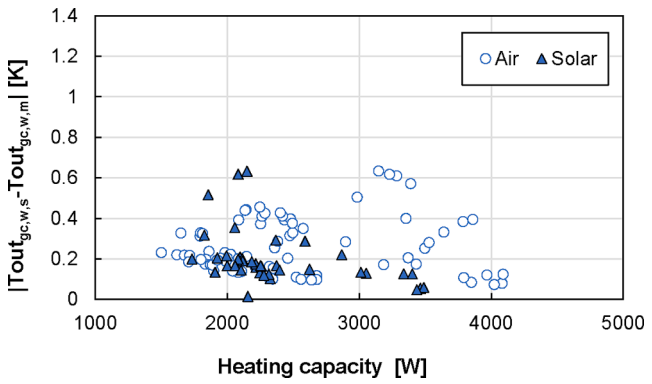

Fig. 5. Comparison between the simulated (s) and measured (m) water temperature values at the gas-cooler outlet as a function of the heating capacity.

- The enthalpy at the inlet of the evaporator is considered to be equal to the enthalpy at the EEV inlet (isenthalpic expansion)

$$h_{in,e} = h_{in,lam} \tag{8}$$

- An updated value of the evaporation temperature is finally obtained, based on the used evaporator and the environmental conditions. When the heat pump works in air-mode, T_e is evaluated by simultaneously solving the energy balance equation at the evaporator (Eq. (9)) and the efficiency characterizing the finned coil evaporator η_e (Eq.10).

$$Q_e = \dot{m}_r(h_{out,e} - h_{in,e}) \tag{9}$$

$$\eta_e = \frac{Q_e}{Q_{max}} = a_1(T_{air} - T_e) + a_2 \tag{10}$$

In Eq. (9), $h_{out,e}$ is also a function of the evaporation temperature T_e. In Eq. (10), Q_{max} is the maximum heat flow rate that the evaporator can exchange, and η_e is calculated with a specific empirical correlation as a function of the air temperature and the evaporation temperature. The coefficients (a_1 and a_2) depend on the fan velocity [24], and their values are reported in Appendix B.

When the heat pump works in solar-mode, the updated value of the evaporation temperature is obtained by solving the PVT evaporator model described in 3.2.2.

- The procedure is repeated until the evaporation temperature reaches a convergence value within a tolerance of 0.01 K. When considering solar-mode operations, the temperature of all the nodes should converge within the fixed tolerance value.

3.2.1. Gas-cooler model

Due to the high variation of the thermophysical properties of the CO_2 in supercritical conditions, the gas-cooler has been modeled using a distributed parameters approach, i.e., considering the temperature and enthalpy variation of the fluid along the heat exchanger length. The model inputs are:

- the refrigerant mass flow rate;
- the refrigerant temperature and pressure at the inlet;
- the water mass flow rate;
- the water temperature at the inlet.

The model outputs are the outlet temperature of the fluids (the pressure drop along the gas-cooler is neglected in the model) and the heating capacity Q_{gc}.

The model considers an equal distribution of the fluids among the channels. Therefore, the problem can be limited to a representative plate where the mass flow rates of the refrigerant and the water are:

$$\dot{m}_{r,p} = \frac{\dot{m}_r}{N/2 - 1} \tag{11}$$

$$\dot{m}_{w,p} = \frac{\dot{m}_w}{N/2} \tag{12}$$

where N is the number of plates.

The representative plate is discretized into n elements in the flow direction, and in each i −th element, the heat flow rate exchanged between the fluids $Q_{gc,i}$ is supposed to be the same:

$$Q_{gc,i} = \left(\frac{Q_{gc}}{N-2}\right) \Big/ n \tag{13}$$

The consequence is that each discretization has a different heat transfer area.

The heat transfer problem in the representative plate is solved sequentially using the logarithmic temperature difference method through an iterative algorithm. The algorithm is described below:

- A value of the water temperature at the outlet of the gas-cooler is guessed $T_{out_{gc},w}$. A guess value of the heating capacity is thus calculated with Eq. (1);
- The representative plate is discretized with Eq (13). At this point, the enthalpy of the supercritical CO_2 and the water at the inlet of each discretized element can be easily obtained with the following equations:

$$h_{in,r,i} = h_{inGC,r} - \frac{Q_{gc,i}}{\dot{m}_{r,p}}(i-1) \tag{14}$$

$$h_{in,w,i} = h_{outGC,w} - \frac{Q_{gc,i}}{\dot{m}_{w,p}}(i-1) \tag{15}$$

Where $h_{outGC,w}$ is calculated with Refprop [34] using the guess value of $T_{out_{gc},w}$. Similar equations can be obtained for the enthalpy at the outlet of each element;

- The average thermophysical properties of the fluids along the plate are calculated based on the local enthalpy and temperature. The local heat transfer coefficient on the refrigerant side $htc_{r,i}$ can be calculated using the new correlation developed by Zendehboudi et al. [32]. The water-side heat transfer coefficient $htc_{w,i}$ is calculated with the well-established Martin correlation [37]. The global heat transfer coefficient in each discretized element is equal to:

$$K_i = \frac{1}{\frac{1}{htc_{r,i}} + \frac{1}{htc_{w,i}} + \frac{t_p}{\lambda_p}} \tag{16}$$

where the last term refers to the heat conduction through the plate with thickness t_p and thermal conductivity λ_p;

- The area of each plate discretization can be calculated based on the mean logarithmic temperature method:

$$A_i = \frac{Q_{gc,i}}{K_i} \frac{\log\left(\frac{T_{out,r,i} - T_{in,w,i}}{T_{in,r,i} - T_{out,w,i}}\right)}{(T_{out,r,i} - T_{in,w,i}) - (T_{in,r,i} - T_{out,w,i})} \tag{17}$$

The total area of the reference plate based on the guess value of the heating capacity is then equal to:

$$A_{p,guess} = \sum_{i=1}^{n} A_i \tag{18}$$

- The guess value of the plate area $A_{p,guess}$ is compared to the actual value A_p: if $A_{p,guess} > A_p$, $T_{out_{gc},w}$ is increased while if $A_{p,guess} < A_p$,

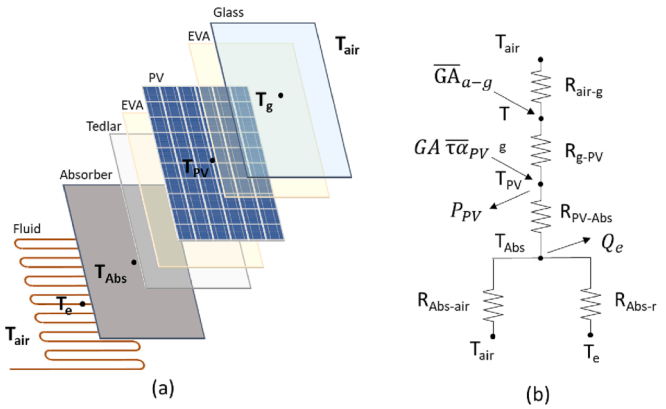

Fig. 6. (a) Section of the PVT model. (b) Scheme of the equivalent electrical network of the PVT model.

$T_{out_{gc},w}$ is decreased. The solution algorithm restarts with the updated value of $T_{out_{gc},w}$ until the percentage difference between $A_{p,guess}$ and A_p is lower than a tolerance value equal to 1%.

The model of the gas-cooler has been validated against experimental data. Fig. 5 reports the agreement between the experimental and calculated values of the water temperature at the outlet of the gas-cooler considering the steady-state data presented by Zanetti et al. [24], referred to the investigated heat pump.

3.2.2. PVT model

The model of the PVT panels is based on the lumped parameter model described and validated in [38]. The original mathematical model simulated an uncovered roll-bond PVT hybrid solar collector. A 1-D lumped-parameter modeling approach was adopted, representing each PVT layer as a thermal node. Heat balance equations were used to calculate the nodes' temperatures and derive the electrical and thermal performance of the solar collectors' field. In this work, 3 PVT panels are used as the evaporator, and the cross-section of the PVT collector (a) and the equivalent electrical circuit of the model (b) are shown in Fig. 6. Similarly to [25], the PVT panel can be divided into three main layers: the protective upper glass, the PV layer, and the absorber plate. These layers correspond to the nodes of the system of resistances to which the fluid node is added. The model evaluates the conduction, convection, and radiation heat fluxes within the different layers of the panel and the external ambient influence [38]. The thermal capacitance of the different nodes is neglected.

The PVT panels model was integrated into the heat pump's model for the TRNSYS type.

The model inputs are:

- the incident solar radiation and the incidence angle of beam radiation;
- the external air temperature and the sky temperature;
- the wind velocity;
- the inlet refrigerant temperature and flow rate.

The outputs are the thermal and electrical power generated by the PVT panel and the outlet refrigerant temperature. In addition, the model calculates the average temperature of each thermal node.

Using the same procedure described in [38], the model evaluates the refraction, absorption, and reflection phenomena and finally derives the incident solar radiation on the PV layer and solves a system of equations at each node of the 1-D network of thermal resistances. The heat balance equations at the different nodes are presented below:

- *The energy balance on the glass node*

The glass node is the first node of the equivalent electrical network represented in Fig. 6. The unknown variables in the energy balance equation (Eq. (19)) are the temperatures T_g and T_{PV}. The first term of the equation is the net solar radiation absorbed by the glass, defined in Eq. (20). In Eq. (20), α_g is the global coefficient of absorption of the glass, ρ_g is the global coefficient of reflection of the glass and $\overline{\tau\alpha}_{PV}$ is the ratio of absorbed solar radiation by the PV cells (Eq. (23)) [39]. The thermal resistance R_{g-PV} (Eq. (21)) depends on the geometry (thickness) and thermal properties (thermal conductivity) of the materials composing the considered layers. H_{g-air} (Eq. (22)) is the global transmission coefficient on the glass surface [40], where ϵ_g is the glass emittance, σ is the Stefan-Boltzmann constant, β is the slope of the PVT panel surface, and v is the wind velocity.

$$\overline{GA}_{a-g} + A\,\frac{T_{PV} - T_g}{R_{g-PV}} - A\,\left(T_g - T_{air}\right)\,H_{g-air} = 0 \tag{19}$$

$$\overline{GA}_{a-g} = GA\alpha_g + GA\left(1 - \alpha_g - \rho_g - \overline{\tau\alpha}_{PV}\right)\alpha_g \tag{20}$$

$$R_{g-PV} = \frac{t_g}{2\lambda_g} + \frac{t_{EVA}}{\lambda_{EVA}} + \frac{t_{PV}}{2\lambda_{PV}} \tag{21}$$

$$H_{g-air} = \epsilon_g\sigma\frac{T_g^4 - T_{sky}^4}{T_g - T_{air}} + 1.247\left[\left(T_g - T_{air}\right)\cos\beta\right]^{\frac{1}{3}} + 2.658v \tag{22}$$

$$\overline{\tau\alpha}_{PV} = \frac{\tau_g\alpha_{PV}}{1 - \rho_d(1 - \alpha_{PV})} \tag{23}$$

- *The energy balance of the PV node*

The energy balance of the PV cell layer is shown in Eq. (24). The thermal resistance R_{PV-Abs} between the PV layer and the absorber plate is a function of the geometry of the system and the thermal properties of the materials (Eq. (25)). The last term represents the energy flux converted into electrical power by the PV system (Eq. (26)). The values of the coefficients η_{PV} and T_{ref-PV} can be found in the PV or PVT panel datasheet and represent the reference efficiency of the PV module at the reference temperature T_{ref-PV}. The value of b_{PV} represents the deviation in efficiency from the reference values.

$$GA\overline{\tau\alpha}_{PV} - A\frac{\left(T_{PV} - T_g\right)}{R_{g-PV}} - A\frac{\left(T_{PV} - T_{Abs}\right)}{R_{PV-Abs}} - P_{PV} = 0 \tag{24}$$

$$R_{PV-Abs} = \frac{t_{PV}}{2\lambda_{PV}} + \frac{2t_{EVA}}{\lambda_{EVA}} + \frac{t_{Tedlar}}{\lambda_{Tedlar}} + \frac{t_{Abs}}{2\lambda_{Abs}} \tag{25}$$

$$P_{PV} = GA\eta_{PV}\left[1 - b_{PV}\left(T_{PV} - T_{ref-PV}\right)\right] \tag{26}$$

- *The energy balance of the absorber plate node*

Eq. (27) shows the energy balance of the absorber plate. The first two terms represent the heat exchanged with the PV layer and the air on the rear side of the panel (Eq. (28)) [40]. The last term is the heat flow rate provided to the refrigerant, and it is calculated with Eq. (9).

$$A\frac{T_{PV} - T_{Abs}}{R_{PV-Abs}} - A(T_{Abs} - T_{air})H_{Abs-air} - Q_e = 0 \tag{27}$$

$$H_{Abs-air} = \epsilon_g\sigma\frac{T_{Abs}^4 - T_{sky}^4}{T_{Abs} - T_{air}} + 1.247[(T_{Abs} - T_{air})\cos\beta]^{\frac{1}{3}} + 2.658v \tag{28}$$

- *The energy balance of the fluid node*

Eq. (29) reports the energy balance equation for the fourth node. Q_e is the heat exchanged between the absorber and the refrigerant, and the

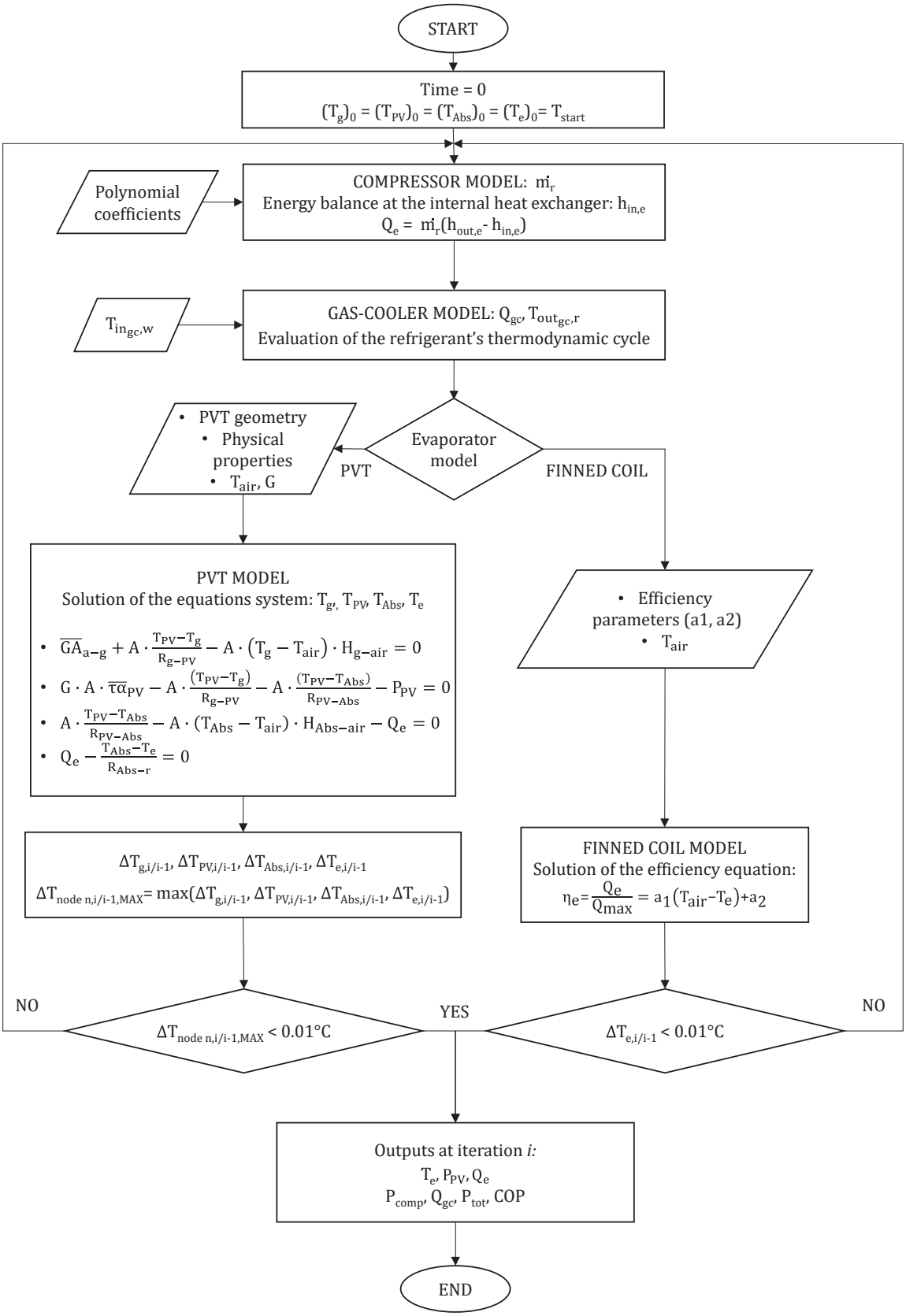

Fig. 7. Flow chart of the PVT model integration in the heat pump model.

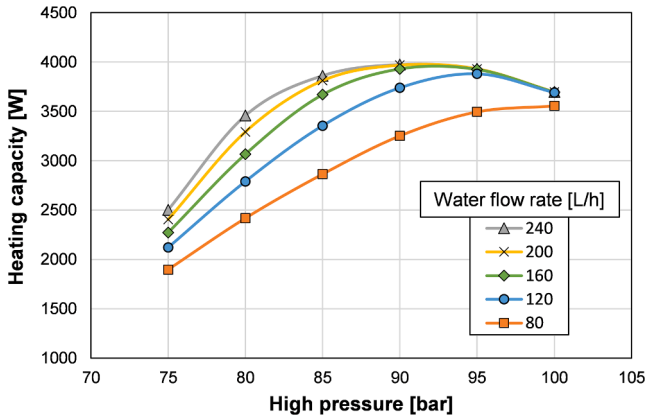

Fig. 8. Calculated values of heating capacity as a function of the high-pressure. Simulations have been realized with the heat pump model in air mode considering a water temperature at the inlet of the gas-cooler equal to 30 °C, air temperature equal to 10 °C and water flow rates between 80 L/h and 240 L/h.

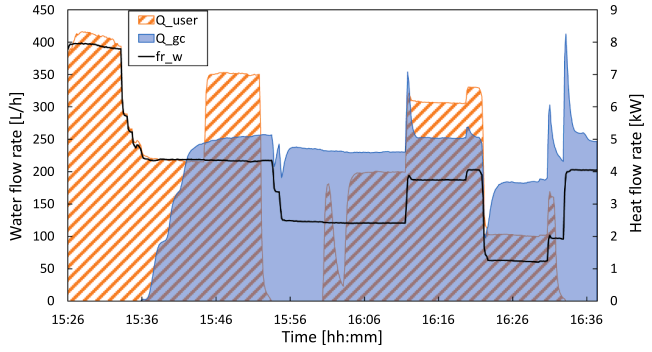

Fig. 9. User thermal load (Q_user), heating capacity (Q_gc), and water flow rate (fr_w) during the experimental test with finned coil evaporator.

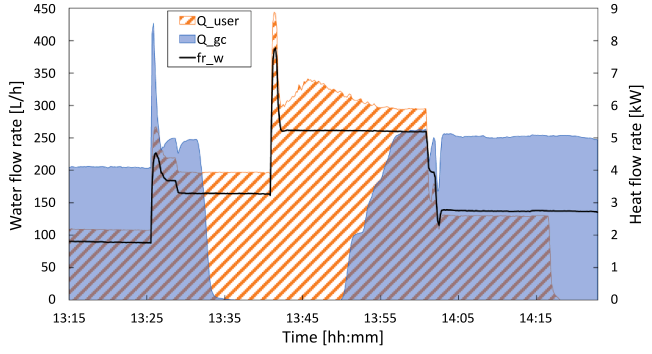

Fig. 10. User thermal load (Q_user), heating capacity (Q_gc), and water flow rate (fr_w) during the experimental test with finned coil evaporator.

second term includes the thermal resistance between the absorber plate and the refrigerant, computed as in Eq. (30).

In Eq. (30), D_{pipe} and l_{pipe} are the hydraulic diameter and the length of the channel, and K is the overall heat transfer coefficient of the pipe, with η_{fin} the fin efficiency. The heat transfer coefficient K_e is evaluated using Eq. (31), where the thermal resistance due to the welding (subscript "we"), the conduction thermal resistance due to the pipe thickness, and the heat transfer coefficient between the fluid and the internal wall (htc_r) are considered. In this work, the value of htc_r is considered constant and equal to 280 W m^{-2} K^{-1}.

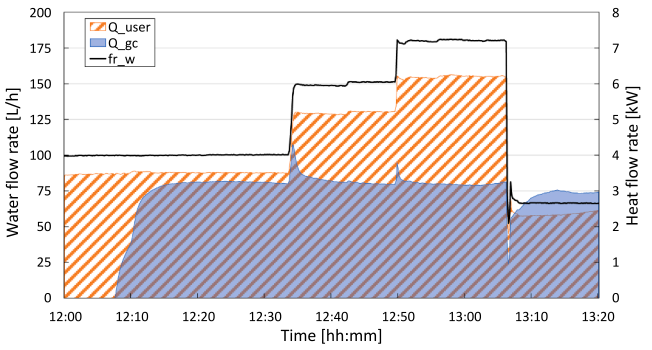

Fig. 11. User thermal load (Q_user), heating capacity (Q_gc), and water mass flow rate (fr_w) during the experimental test with PVT collectors.

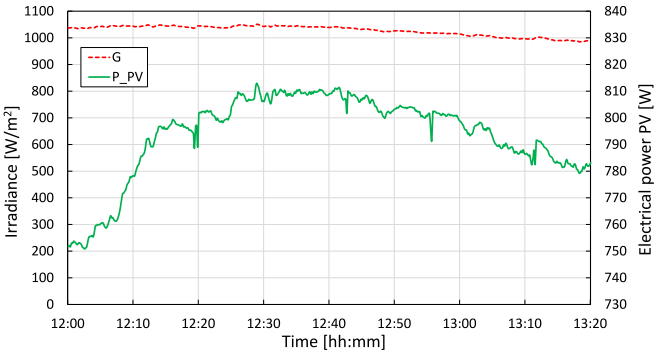

Fig. 12. Global Tilted Irradiance (G) and photovoltaic power production (P_PV) during the experimental test with PVT collectors.

$$Q_e - \frac{T_{Abs} - T_e}{R_{Abs-r}} = 0 \tag{29}$$

$$R_{Abs-r} = \frac{4}{\pi D_{pipe} l_{pipe} K_e \eta_{fin}} \tag{30}$$

$$K_e = \left(\frac{1}{htc_r} + \frac{t_{we}}{\lambda_{we}} + \frac{t_{pipe}}{\lambda_{pipe}} \right)^{-1} \tag{31}$$

The temperatures of the thermal nodes are monitored during two consecutive iterations to ensure the thermal equilibrium in each node is reached. Once the temperature difference between two successive iterations at each node ($\Delta T_{node\ n,i/i-1}$) is computed, the iteration process stops when the maximum $\Delta T_{node\ n,i/i-1}$ is lower than a set tolerance (i.e., 0.01 K).

A flow chart summarizing the main steps of the PVT model integrated into the heat pump model is shown in Fig. 7.

4. Experimental tests

The experimental tests have been carried out in transient conditions to simulate a variable thermal load at the user heat exchanger in real environmental conditions. Each experimental test lasts for 6 h. The experimental tests have been conducted according to the following conditions:

11. Provide water to the user with a temperature not below 45 °C, monitoring the value of the thermocouple at the bottom of TANK2 depicted in Fig. 1;
21. The heat pump switches on when the water temperature measured by the thermocouple positioned in the middle of TANK2 is below 50 °C to ensure the fulfillment of condition c1,

Table 4
Comparison between the steady-state performance of the heat pump in air mode and solar mode.

Compressor speed [%]	Source	Air temp. [°C]	Fan speed [%]	Solar irradiance [W m^{-2}]	Evaporation temp. [°C]	COP/COP$_{air}$ [-]
50	Air	14	50	–	3.5	1
	Solar	14.2	–	808	5.3	1.09
100	Air	14.4	100	–	1.7	1
	Solar	15.3	–	1060	−7.3	0.88

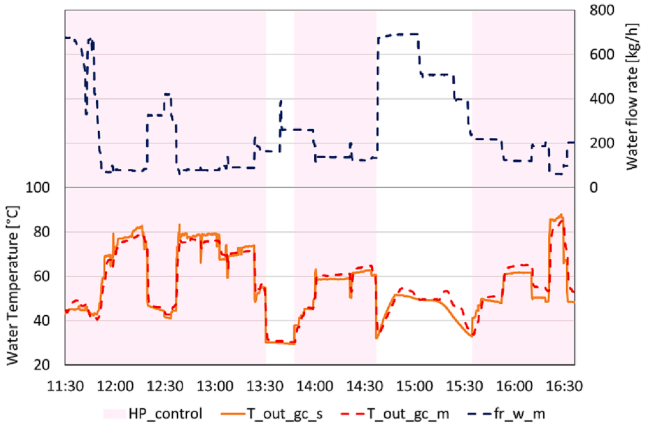

Fig. 13. Water temperature at the gas-cooler outlet, simulated (s) and measured (m) data comparison, and measured water mass flow rate (fr). The finned coil is used as the evaporator. HP_control highlights when the compressor is on.

Fig. 15. Water temperature at the gas-cooler outlet, simulated (s) and measured (m) data comparison, and measured water mass flow rate (fr). PVT panels are used as the evaporator. HP_control highlights when the compressor is on.

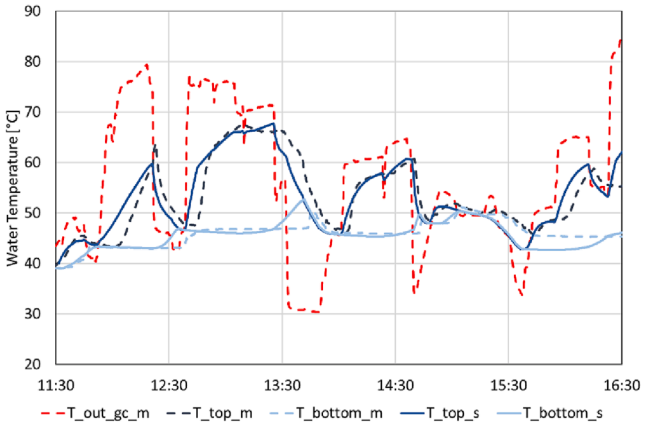

Fig. 14. Simulated (s) and measured (m) data comparison of water temperature at the TANK2 bottom and top nodes and water temperature at the gas-cooler outlet. The finned coil is used as the evaporator.

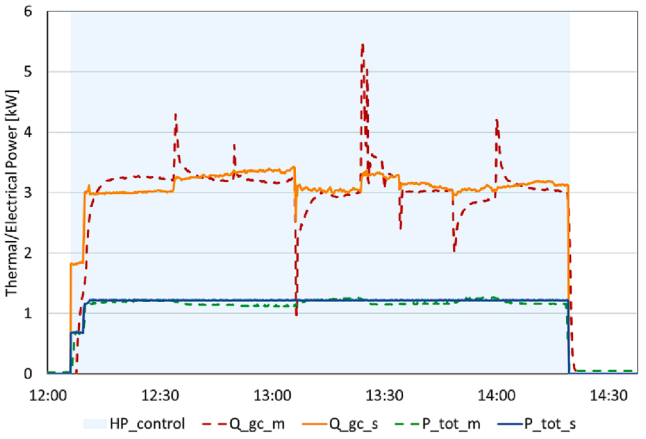

Fig. 16. Heating capacity in the gas-cooler and electrical power overall absorbed by the heat pump, simulated (s) and measured (m) data comparison. PVT panels are used as the evaporator. HP_control highlights when the compressor is on.

considering the inertia of the system and the necessary time for the compressor to start and reach the maximum speed;

31. The heat pump is switched off when the thermocouple positioned at the half-height of TANK2 records a temperature value equal to 55 °C;
41. When the heat pump works in air-mode, the compressor operates at the maximum speed and the fan of the finned coil heat exchanger at the maximum velocity, while in solar-mode the compressor speed has been fixed at the 75% of the full speed;
51. The inlet water temperature at the gas-cooler has been kept in the range between 27 °C and 31 °C (when necessary, the temperature in the TANK1 was regulated by turning on/off the electrical resistances);
61. The electronic expansion valve, which works as a back-pressure valve, automatically regulates the high-pressure. The high-pressure is often optimized for achieving the maximum COP or heating capacity, as a function of the temperature of the refrigerant at the outlet of the gas-cooler and evaporation temperature (Sarkar et al. [41]). In this study, the high pressure was fixed at 95 bar to maintain high values of heating capacity Q_{gc} considering the water operative conditions. Fig. 8 reports the calculated heating capacity as a function of the pressure at the gas-cooler for various mass flow rates, when the water temperature at the inlet of the gas-cooler is equal to 30 °C and the air temperature is equal to 10 °C. It can be observed that the maximum heating capacity is between 90 bar and 100 bar, depending on the water flow rate.

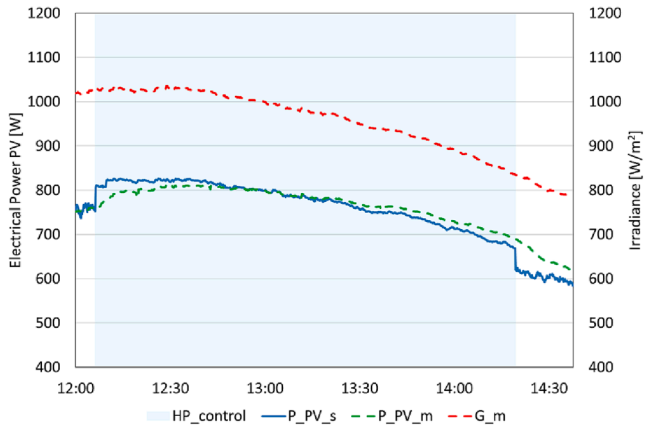

Fig. 17. Global Tilted Irradiance (G) and photovoltaic power production (P_{PV}), simulated (s) and measured (m) data comparison. PVT panels are used as the evaporator. HP_control highlights when the compressor is on.

Figs. 9 and 10 show the user thermal load (Q_{user}), the heating capacity (Q_{gc}), and the water flow rate (fr_w) during two-time intervals of the same test day when the heat pump was working in air-mode, and the ambient temperature was between 9 °C and 11 °C.

Fig. 9 shows the experimental results when the heat pump is turned on (at time 15:36) to satisfy condition c2. The time needed by the heat pump to reach the maximum heating capacity is equal to 5 min. This is an operative condition in which both Q_{user} and Q_{gc} can be present at the same time. The maximum water flow rate is 400 L/h, while the minimum stable value is 80 L/h, and the maximum heating capacity is 5 kW (excluding the peak values due to sudden changes in the water flow rate). The maximum user thermal load is 8 kW when the heat pump is off and 7 kW when the heat pump is on. At 15:50 and 16:30, the USER heat exchanger was isolated for a few minutes, closing the relative valves to simulate a no-user load condition. Still, the heat pump continues to work because the temperature in the TANK2 does not meet condition c3.

Fig. 10 shows an experimental test with the user's continuous thermal load request while the heat pump was switched off from 13:35 to 13:50 because condition c6 was satisfied. The water flow rate ranges from 80 L/h to 260 L/h, the maximum heating capacity is 5 kW, and the maximum user thermal load is around 7 kW. The time needed to switch off the heat pump is very short, about 1 min. From these two tests, it is possible to see that, in general, a change in the water flow rate has more effect on the user thermal load than the heating capacity due to the single loop of the water circuit.

Fig. 11 presents an experimental test using the PVT collectors as the evaporator. In particular, it shows the values of the user's thermal load, the heating capacity, and the water flow rate. During the test, the water flow rate ranges from 66 L/h to 180 L/h, the maximum heating capacity is 3 kW, and the maximum user thermal load is 6 kW. Compared to the air-mode tests, in this case, the heating capacity produced at the gas-cooler is reduced because the compressor speed has been fixed at the 75% of the maximum speed (as reported in condition c4). Likewise, in the air-mode tests, the time needed by the heat pump to reach a constant value of the heating capacity is equal to 5 min.

Fig. 12 reports the photovoltaic power production (P_{PV}) and the global tilted irradiance (GTI) during the test. At the beginning of the test, the power production was equal to 750 W, and the heat pump was turned off. The photovoltaic power production rapidly increases to 810 W (about + 8%) after the switch-on of the heat pump due to the cooling effect of the refrigerant evaporating in the sheet and tube heat exchangers coupled to the PV panels.

Besides the tests in transient conditions, some steady-state tests have been conducted to compare the performance of the heat pump when working in solar and in air modes. Table 4 reports the experimental data obtained in steady-state conditions: tests realized at controlled temperature lift at the gas-cooler ($\Delta T = 5$ K), water inlet temperature equal to 30 °C, high pressure equal to 80 bar, compressor speed equal to 50% and 100%. It can be observed that at partial load (compressor speed equal to 50%), the COP obtained when working with the solar evaporators is higher compared to the one in air mode. In this operative condition, the refrigerant absorbs heat from the PV cells, which are heated by solar radiation, and the evaporation temperature is 1.8 K higher compared to the one in air mode. On the contrary, at full load (compressor speed equal to 100%), the collectors' area is undersized and the evaporation temperature drastically decreases compared to air mode, reducing also the COP.

The problem of collectors sizing and switching between the solar and air source is thus crucial for dual-source heat pump system. This topic has been partially investigated in a previous study using a steady-state model [24]. However, for the optimization in real operative conditions, the heat pump unit together with the hydronic circuit should be taken into account. Therefore, the dynamic model presented in Section 3 can represent a powerful tool for long-term performance analysis. Section 5 presents, the validation of the model.

5. Model validation

This section presents and discusses the comparison between measurements and TRNSYS model results.

A preliminary calibration of the model's plant was performed using data from the monitoring campaign. The calibration was carried out by tuning some tanks' parameters: the number of isothermal nodes in which the two storages are subdivided and the position of the inlet and outlet nodes. This modulization choice affects the simulation of the fluid's stratification inside the storage and its temperature at the outlet. The final selection was made by observing the root mean square error (RMSE) of the water temperature at the outlet of the two tanks. The best results have been obtained by subdividing TANK1 into nine nodes and TANK2 into twelve nodes, where nodes are numbered starting from the upper part of the thermal storages, which are 1.4 m high. Node 8 of TANK1 is where the inlet port is located in the model, while the outlet port is placed in Node 1. In the same way, in TANK2, the inlet port is placed in node 2, and the outlet port is in node 12. The RMSE equal to 7.2% for TANK1 and 3.6% for TANK2 has been obtained with these assumptions for the case where the finned coil is used as the evaporator.

5.1. Finned coil simulations

Figs. 12 to 13 show the model's results when the heat pump operates with the finned coil heat exchanger on the same test day reported in Figs. 4 and 5. Dashed lines represent measured data, while continuous lines represent the results of the simulations. The shaded areas in the figures show the periods when the heat pump is ON.

In particular, Fig. 13 presents the water temperature at the gas-cooler outlet and the water flow rate. The trends of the measured and simulated temperatures are consistent, showing a maximum deviation of about 3 °C. As shown in Fig. 13, the gas-cooler outlet temperature strongly depends on the water mass flow rate circulating in the system.

Fig. 14 shows the water temperature measured and simulated at the TANK2 level. In particular, the water temperature at the gas-cooler outlet (i.e., TANK2 inlet) is shown and compared with the temperature in the top and bottom parts of the thermal storage. Due to the tank's thermal stratification, a time shift in the water temperature peaks can be seen between the entering temperature and the outlet temperature of the storage. The results obtained from the model in TRNSYS are in good agreement with the measured data. The maximum temperature deviation is around 5 °C, related to higher thermal inertia and faster reaction to the flow rate variation of the system simulated by the model, compared to the experimental data, which results in a longer delay of the thermal response.

Temperature differences observed at the TANK2 outlet also affect the

temperature at the outlet of the other components of the plant. Indeed, the temperature at the outlet of the plate heat exchanger and the water temperature exiting the mixing valve present the same trend, in slight advance compared to the measured data.

5.2. PVT simulations

The same analysis was carried out on the heat pump using the PVT as the evaporator. In the following figures, dashed lines represent measured data, while continuous lines represent the results of the simulations. The shaded areas in the figures show the periods when the heat pump is ON.

The calibrated model of the hydronic circuit was used to perform the dynamic simulations. Fig. 15 shows the water temperature at the gas-cooler outlet and the water flow rate when the heat pump is coupled to the PVT panels. The trends of the simulated temperature and measured temperature are in good agreement. The maximum deviation is observed in correspondence to the heat pump switching on and when sudden changes in the water flow rate occur. Indeed, in these operative conditions, the model does not accurately simulate the inertia of the unit, which, in real applications, does not immediately respond to the water flow rate variation or reach full power instantaneously after being switched on.

Fig. 16 shows the simulated and measured thermal power produced by the heat pump and exchanged in the gas-cooler and the electrical power overall absorbed by the heat pump. The agreement between measured and simulated data is good, with a relative error lower than 10% in both values.

The coefficient of performance (COP) can be calculated as the thermal energy produced by the heat pump divided by the electrical energy absorbed. The COP obtained from the experimental tests is equal to 2.63 when considering the period in which the heat pump is ON and equal to 2.43 when the standby phase is also considered (during the standby phase, only the electronics of the heat pump are active). The simulated COP, when the heat pump is ON, is equal to 2.58, less than 2% lower than the value obtained through the experimental campaign.

In conclusion, Fig. 17 shows the measured and simulated value of the photovoltaic power production, together with the Global Tilted Irradiance. Also, in this case, the agreement between simulated and measured data is good, both when the heat pump is ON and the evaporating CO_2 cools the PVT panels and when the heat pump is OFF with no PV cells cooling. The PVT model does not consider the thermal capacitance of the solar collectors and cannot simulate the thermal inertia of the panels. This can be observed in Fig. 17, where, around 14:20, the heat pump is switched off, and the simulated electrical power production drastically decreases due to the instantaneous increase in the PV cells' temperature, which penalizes the PV electrical efficiency.

6. Conclusion

This work presents experimental tests and dynamic simulations of a dual-source (solar and air) CO_2 heat pump system for hot water provision. The heat pump can work alternatively with two evaporators: a conventional finned coil heat exchanger or three photovoltaic-thermal (PVT) collectors. The main results are as follows:

- Experimental tests on the heat pump have been conducted in dynamic conditions both in air and solar modes. When operating in solar mode, the experimental tests showed an 8% increase in photovoltaic power production due to the cooling effect of the refrigerant evaporating in the collectors.
- A novel TRNSYS Type modeling of the dual-source heat pump was developed. The transcritical CO_2 cycle was modeled using an internal link to REFPROP. In addition, the mathematical models of the gas-cooler and the PVT panels included in the TRNSYS type were compared against experimental data.
- The dynamic model, simulating the operating conditions of the dual-source heat pump prototype and the hydronic circuit, was preliminary calibrated and then validated against experimental data collected in air-mode and solar-mode.
- The temperature values at the inlet and outlet of the hydronic system's components are in good agreement with the measured data. Moreover, concerning the gas-cooler heating capacity, the electrical power absorbed by the heat pump, and the electrical power produced by the PVT collectors, the error between experimental data and simulation results is considered acceptable.
- In solar mode, the simulated COP of the heat pump was 2.58, 2% lower than the value estimated through the experimental campaign.

In conclusion, the validated model is a useful tool for performing seasonal simulations of a CO_2 heat pump operating in solar and air modes. Future works will focus on developing a control strategy to select the thermal sources to maximize the benefits of a similar dual-source system.

Declaration of Competing Interest

The authors declare that they have no known competing financial interests or personal relationships that could have appeared to influence the work reported in this paper.

Data availability

Data will be made available on request.

Acknowledgments

This work has been realized with the support of CSEA (Cassa per i servizi energetici e ambientali) through the project CCSEB_00075 – SOLAIR-HP. The Department of Industrial Engineering of the University of Padova is acknowledged for the financial support through the BIRD 228237.

The Authors would like to thank Alberto Scotton for his contribution in the preliminary phase of this work.

Appendix A

The refrigerant mass flow rate $\dot{m}_r$, the compressor power consumption P_{tot} and the specific compressor work ($h_{dis} - h_{suc}$) are calculated with three-variable polynomial of three degree, depending by the evaporation temperature, the pressure at the gas-cooler and the compressor speed. The correlations have been developed from data collected on the present heat pump during the steady-state operations and have the following form:

$$Y = C_0 V_c + C_1 V_c^2 + C_2 p_{gc} + C_3 p_{gc} V_c + C_4 p_{gc} V_c^2 + C_5 p_{gc}{}^2 + C_6 p_{gc}{}^2 V_c + C_7 T_e + C_8 T_e V_c + C_9 T_e V_c^2 + C_{10} T_e p_{gc} + C_{11} T_e p_{gc} V_c + C_{12} T_e p_{gc}{}^2 + C_{13} T_e^2 + C_{14} T_e^2 V_c + C_{15} T_e^2 p_{gc} + C_{16} + C_{17} T_e^3 + C_{18} p_{gc}{}^3 + C_{19} V_c^3$$

The 20 experimental coefficients are reported in Table A.

Table A
Polynomial coefficients.

Coefficient	$\dot{m}_r$[kg s^{-1}]	P_{tot} [W]	$h_{dis} - h_{suc}$[J kg^{-1}]
C_0	2.1378E-04	15.875031	1399.536
C_1	4.0078E-06	−0.002027	−11.7847
C_2	6.0166E-03	−155.280760	18801.46
C_3	5.0876E-06	−0.202369	−7.80721
C_4	2.4859E-08	0.000579	−0.00559
C_5	7.9568E-05	2.141396	−215.654
C_6	5.0575E-08	0.001558	0.04707
C_7	−5.7330E-03	−41.537614	3622.331
C_8	2.8598E-05	0.151075	−70.6871
C_9	−1.6117E-07	−0.004827	0.338169
C_{10}	1.2026E-04	0.671789	−46.3325
C_{11}	−4.6856E-08	0.005275	0.139106
C_{12}	−6.7132E-07	−0.005014	0.150359
C_{13}	3.8703E-05	0.754221	−78.4838
C_{14}	6.3211E-07	−0.012471	0.986062
C_{15}	1.9526E-08	−0.003393	0.162309
C_{16}	1.5280E-01	3554.000800	−548464
C_{17}	−5.9969E-07	−0.013690	−1.31049
C_{18}	−3.5140E-07	−0.009338	0.849855
C_{19}	−1.2061E-08	−0.000065	0.054633

Appendix B

The efficiency characteristic of the finned coil evaporator is described by the following equation:

$$\eta_e = \frac{Q_e}{Q_{max}} = a_1(T_{air} - T_e) + a_2$$

The coefficients a_1 and a_2 have been obtained during a previous experimental campaign [24]. Their values are reported in Table B.

Table B
Finned coil evaporator coefficients.

	Fan speed			
Coefficient	25%	50%	75%	100%
a_1 [K^{-1}]	0.02	0.026	0.022	0.013
a_2 [-]	0.44	0.21	0.22	0.20

References

[1] IEA, Renewables 2021, Int. Energy Agency Publ. Int., p. 167, 2021.
[2] IEA, Heating, Paris, 2022.
[3] IEA, The Future of Heat Pumps, Paris, 2022.
[4] European Commision, Commission delegated regulation (EU) 2022/759, Off. J. Eur. Union, 2022.
[5] "Fuel Mix." [Online]. Available: https://www.gse.it/servizi-per-te/fonti-rinnovabili/fuel-mix. [Accessed: 28-Dec-2022].
[6] M. Schulz, D. Kourkoulas, Regulation (EU) No 517/2014 of the European Parliament and of the Council of 16 April 2014 on fluorinated greenhouse gases and repealing Regulation (EC) No 842/2006, Off. J. Eur. Union, 2014.
[7] United Nations, Kigali Amendment to the Montreal Protocol On Substances that Deplete the Ozone Layer. 2016.
[8] M.H. Kim, J. Pettersen, C.W. Bullard, Fundamental process and system design issues in CO2 vapor compression systems, Prog. Energy Combust. Sci. 30 (2) (Jan. 2004) 119–174.
[9] R.U. Rony, H. Yang, S. Krishnan, J. Song, Recent advances in transcritical CO 2 (R744) heat pump system, A review 12 (3) (2019) pp.
[10] F. Calise, F.L. Cappiello, L. Cimmino, M. Dentice d'Accadia, M. Vicidomini, Dynamic modelling and thermoeconomic analysis for the energy refurbishment of the Italian building sector: Case study for the 'Superbonus 110 %' funding strategy, Appl. Therm. Eng. 213 (Aug. 2022), 118689.
[11] TRNSYS : Transient System Simulation Tool. [Online]. Available: http://www.trnsys.com/. [Accessed: 18-Feb-2019].
[12] X. Liu, Y. Hu, Q. Wang, L. Yao, M. Li, Energetic, environmental and economic comparative analyses of modified transcritical CO2 heat pump system to replace R134a system for home heating, Energy 229 (2021), 120544.
[13] L.W. Yang, et al., Review of the advances in solar-assisted air source heat pumps for the domestic sector, Energy Convers. Manag. 247 (2021), 114710.
[14] T. Kim, B.-I. Choi, Y.-S. Han, K.H. Do, A comparative investigation of solar-assisted heat pumps with solar thermal collectors for a hot water supply system, Energy Convers. Manag. 172 (2018) 472–484.
[15] G. Emmi, S. Bordignon, A. Zarrella, M. De Carli, A dynamic analysis of a SAGSHP system coupled to solar thermal collectors and photovoltaic-thermal panels under different climate conditions, Energy Convers. Manag. 213 (2020) 112851.
[16] J. Zhou, C. Zeng, Z. Wang, W. Lyu, Y. Tang, D. Wu, W. Ji, Y. Yuan, Indirect expansion solar assisted heat pump system: a review, Sustain. Energy Technol. Assessments. 53 (2022) 102409.
[17] F. Leonforte, A. Miglioli, C. Del Pero, N. Aste, N. Cristiani, L. Croci, G. Besagni, Design and performance monitoring of a novel photovoltaic-thermal solar-assisted heat pump system for residential applications, Appl. Therm. Eng. 210 (2022) 118304.
[18] X. Yu, Z. Guo, Z. Gao, B. Yang, X. Ma, S. Dong, Thermodynamic investigation of a direct-expansion solar assisted heat pump with evacuated tube collector-evaporator, Renew. Energy 206 (2023) 418–427.
[19] W.M. Duarte, S.N. Rabelo, T.F. Paulino, J.J.G. Pabón, L. Machado, Experimental performance analysis of a CO2 direct-expansion solar assisted heat pump water heater, Int. J. Refrig. 125 (May 2021) 52–63.
[20] T.d.F. Paulino, R.N. de Oliveira, A.A.T. Maia, B. Palm, L. Machado, Modeling and experimental analysis of the solar radiation in a CO2 direct-expansion solar-assisted heat pump, Appl. Therm. Eng. 148 (2019) 160–172.
[21] S. Vaishak, P.V. Bhale, Photovoltaic/thermal-solar assisted heat pump system: Current status and future prospects, Solar Energy 189 (2019) 268–284.
[22] B. Du, Z. Quan, L. Hou, Y. Zhao, X. Lou, C. Wang, Experimental study on the performance of a photovoltaic/thermal-air dual heat source direct-expansion heat pump, Appl. Therm. Eng. (2021).
[23] J. Zhou, X. Ma, X. Zhao, Y. Yuan, M. Yu, J. Li, Numerical simulation and experimental validation of a micro-channel PV/T modules based direct-expansion solar heat pump system, Renew. Energy 145 (2020) 1992–2004.
[24] E. Zanetti, M. Azzolin, S. Girotto, D. Del Col, Performance and control of a CO2 dual source solar assisted heat pump with a photovoltaic-thermal evaporator, Appl. Therm. Eng. 218 (2023) 119286.
[25] E. Zanetti, M. Azzolin, R. Conte, S. Girotto, D. Del Col, Experiments and dynamic modelling of dry expansion and flooded evaporators in a CO2 solar assisted heat pump, Appl. Therm. Eng. 217 (2022) 118964.
[26] Z. Han, M. Zheng, F. Kong, F. Wang, Z. Li, T. Bai, Numerical simulation of solar assisted ground-source heat pump heating system with latent heat energy storage in severely cold area, Appl. Therm. Eng. 28 (11–12) (2008) 1427–1436.
[27] E. Zanetti, S. Bonduà, S. Bortolin, V. Bortolotti, M. Azzolin, F. Tinti, Sequential coupled numerical simulations of an air/ground-source heat pump: Validation of

the model and results of yearly simulations, Energy Build. 277 (Dec. 2022), 112540.
[28] S. Sinha, S.S. Chandel, Review of software tools for hybrid renewable energy systems, Renew. Sustain. Energy Rev. 32 (2014) 192–205.
[29] S. Bordignon, G. Emmi, A. Zarrella, M. De Carli, Energy analysis of different configurations for a reversible ground source heat pump using a new flexible TRNSYS Type, Appl. Therm. Eng. 197 (Oct. 2021), 117413.
[30] R. Chargui, H. Sammouda, A. Farhat, Geothermal heat pump in heating mode: Modeling and simulation on TRNSYS, Int. J. Refrig. 35 (7) (Nov. 2012) 1824–1832.
[31] J. Ma, A. S. Fung, M. Brands, N. Juan, O. Mohammad Abul Moyeed, Performance analysis of indirect-expansion solar assisted heat pump using CO2 as refrigerant for space heating in cold climate, Sol. Energy, vol. 208, pp. 195–205, Sep. 2020.
[32] A. Zendehboudi, Z. Ye, A. Hafner, T. Andresen, G. Skaugen, Heat transfer and pressure drop of supercritical CO2 in brazed plate heat exchangers of the tri-partite gas cooler, Int. J. Heat Mass Transf. 178 (Oct. 2021), 121641.
[33] Joint Committee For Guides In Measurements, Evaluation of measurement data — Guide to the expression of uncertainty in measurement, Int. Organ. Stand. Geneva ISBN, 2008.
[34] E.W. Lemmon, M.L. Huber, M.O. Mclinden, REFPROP 10.0, NIST Stand. Ref. database (2018).
[35] BSI Standards Publication Refrigerant compressors — Rating conditions , tolerances and presentation of manufacturer ' s performance data, 2013.
[36] AHRI, AHRI Standard 540: Performance rating of positive displacement refrigerant compressors, 2020.
[37] H. Martin, A theoretical approach to predict the performance of chevron-type plate heat exchangers, Chem. Eng. Process. Process Intensif. 35 (4) (1996) 301–310.
[38] A. Zarrella, G. Emmi, J. Vivian, L. Croci, G. Besagni, The validation of a novel lumped parameter model for photovoltaic thermal hybrid solar collectors: a new TRNSYS type, Energy Convers. Manag. 188 (May 2019) 414–428.
[39] BS EN ISO 9806, BS EN ISO 9806: 2017 Solar energy. Solar thermal collectors. Test methods, British Standards. BSI Standards Limited 2018, 2017.
[40] C.H. Cox, P. Raghuraman, Design considerations for flat-plate-photovoltaic/thermal collectors, Sol. Energy 35 (3) (1985) 227–241.
[41] J. Sarkar, S. Bhattacharyya, M.R. Gopal, Optimization of a transcritical CO2 heat pump cycle for simultaneous cooling and heating applications, Int. J. Refrig. 27 (8) (2004) 830–838.